Orthogonally woven 3D nanofiber scaffolds promote rapid soft tissue regeneration by enhancing bidirectional cell migration

Jiayi Yuan [a,b,1], Bingbing Sun [b,c,1], Weixing Ma [a,**], Chao Cai [b], Zhenzhen Huang [b], Peiyi Zhou [d], Lei Yi [e,***], Lubin Liu [d,****], Shixuan Chen [b,*]

[a] School of Pharmacy, Jiangsu Ocean University, Lianyungang, 222005, China
[b] Zhejiang Engineering Research Center for Tissue Repair Materials, Wenzhou Institute, University of Chinese Academy of Sciences, Wenzhou, Zhejiang, 325001, China
[c] Department of Critical Care Medicine, The Air Force Characteristic Medical Center, Air Force Medical University, Beijing, 100000, China
[d] Chongqing Health Center for Women and Children, Chongqing Obstetric and Gynecologic Hospital, Chongqing, China
[e] Department of Burn, Ruijin Hospital, Shanghai Jiao Tong University School of Medicine, Shanghai, 200025, China

ARTICLE INFO

ABSTRACT

Repairing large-area soft tissue defects caused by traumas is a major surgical challenge. Developing multifunctional scaffolds with suitable scalability and favorable cellular response is crucial for soft tissue regeneration. In this study, we developed an orthogonally woven three-dimensional (3D) nanofiber scaffold combining electrospinning, weaving, and modified gas-foaming technology. The developed orthogonally woven 3D nanofiber scaffold had a modular design and controlled fiber alignment. In vitro, the orthogonally woven 3D nanofiber scaffold exhibited adjustable mechanical properties, good cell compatibility, and easy drug loading. In vivo, for one thing, the implantation of an orthogonally woven 3D nanofiber scaffold in a full abdominal wall defect model demonstrated that extensive granulation tissue formation with enough mechanical strength could promote recovery of abdominal wall defects while reducing intestinal adhesion. Another result of diabetic wound repair experiments suggested that orthogonally woven 3D nanofiber scaffolds had a higher wound healing ratio, granulation tissue formation, collagen deposition, and re-epithelialization. Taken together, this novel orthogonally woven 3D nanofiber scaffold may provide a promising and effective approach for optimal soft tissue regeneration.

1. Introduction

Human soft tissues, including skin [1], connective tissues, and muscles [2], are not homogeneous or isotropic [3,4]. Instead, these tissues exhibit regional and directional anisotropy in the spatial structure. For example, the structure of the linea alba, anterior and posterior rectus sheaths in the abdominal wall shows a structural heterogeneity [5]. The structural heterogeneity seen in living tissues arises from the preferred alignment of extracellular matrix (*e.g.*, collagen fibers, elastin fibers, laminin fibers, and fibronectin fibers) and/or cells [6]. This alignment imparts designated functionalities to these tissues. Compared

with isotropic scaffolds, structural heterogeneity scaffolds exhibit enhanced mechanical properties and cell movement along the orientation direction [7]. For repairing these structure heterogeneous soft tissues, their anisotropic structural characteristics (*i.e.*, mimicking the orientation of the collagen fibers) should be considered when designing the scaffold.

Many efforts have been made to prepare structure heterogeneous scaffolds for tissue engineering and regenerative medicine [8]. For instance, Guilak et al. presented a microscale 3D weaving technique to create anisotropic 3D woven structures mixed with a chondrocyte–hydrogel mixture to engineer cartilage tissue in vitro [9].

Fig. 1. Schematic illustrates the applications of orthogonally woven 3D nanofiber scaffold in soft tissue regeneration. For one thing, the orthogonally woven 3D nanofiber scaffold could mimic the abdominal muscle tissue consisting of biaxially-aligned muscle fibers. It can potentially be used for hernia repair. For another, the orthogonally woven 3D nanofiber scaffold is able to recruit cells (*e.g.*, fibroblasts, endothelial cells, and macrophages) from four directions simultaneously, and it is expected to be used to repair skin wounds.

However, the above 3D woven structures contained a mass of dense microfibers, which will hinder cell penetration. Advincula et al. developed a 3D printed heterogeneous polyurethane/Poly(lactic acid)-/graphene oxide nanocomposites for tissue regeneration applications [10]. The porosity of the 3D-printed scaffold is too high, leading to low cell seeding efficiency. In addition, the basic scale sizes of the woven fiber and printed scaffold are micro- or milli-meters, which are still much larger than collagen nanofibers, the fundamental units of the human extracellular matrix. To address the above limitations, Xie et al. reported a simple approach to prepare structure heterogeneous 3D nanofiber scaffolds with a basket-woven structure composed of uniaxially aligned electrospun nanofiber strips [11]. While the compact nanofiber strips may impede cell infiltration and lead to prolonged degradation, potentially resulting in significant tissue rejection issues.

Our previous study invented a new method for preparing 3D nanofiber scaffolds with controlled fiber orientation and porosity by combining electrospinning and modified gas-foaming technology [12–14]. The hierarchically assembled nanofiber scaffold exhibits excellent tissue repair capabilities due to its ability to rapidly recruit cells, enabled by the directional fiber alignment [15,16]. Thus, we hypothesize that we can first weave nanofiber strips into 2D orthogonally woven scaffolds and then expand each of these woven nanofiber strips into a 3D nanofiber scaffold. This process yields an orthogonally woven 3D scaffold with bidirectionally aligned electrospun nanofibers. This approach achieves structural heterogeneity, and the bidirectional 3D nano-topography offers advantages over 2D uniaxial alignment for improved cell recruitment. The bidirectionally aligned 3D nanofibers can more quickly guide cell migration from surrounding healthy tissue to the defect area (Fig. 1). In the presented study, we will explore the preparation of the orthogonally woven 3D nanofiber scaffolds, the scaffold's mechanical properties, and their role in diabetic skin wound healing and hernia repair. Besides, we used Lando and PELNAC as positive controls, which are widely used isotropic scaffolds for wound healing in clinics.

2. Materials and methods

2.1. Materials and reagents

Polycaprolactone (PCL) (catalog number: S26795) used in the experiments was purchased from Shanghai Yuanye Bio-Technology (Shanghai, China). Dichloromethane (DCM) (catalog number:75-09-2) was purchased from Tansoole (Shanghai, China). N, N-Dimethylformamide (DMF) (catalog number:68-12-2) was purchased from Sigma-Aldrich (MO, USA). F127 (catalog number: P822479) was purchased from Macklin (Shanghai, China). Sodium borohydride (catalog number: KM0010) was purchased from Komeo (Tianjin, China), and PBS (catalog number: C10010500BT) was purchased from Gibco (USA). Dulbecco's modified eagle medium (DMEM) (catalog number: 11965118), penicillin-streptomycin (PS) (catalog number: 15140122), and fetal bovine serum (FBS) (catalog number:10099-141C) were ordered from Invitrogen (CA, USA). Paraformaldehyde (catalog number: 30525-89-4) was ordered from Aladdin (Shanghai, China). Paraffin (catalog number: 8002-74-2) was purchased from Sigma-Aldrich (MO, USA). The Hematoxylin & Eosin staining kit (H&E) (catalog number: ZY61872FA) was purchased from Zeye Biotechnology (Shanghai, China). Masson (catalog number: MST-8003) was purchased from Maxim Reagent (Fuzhou, China). Chloral hydrate (catalog number: R00634) was purchased from Leagene (Beijing, China). STZ (catalog number: 60256ES76) was purchased from Yeasen (Shanghai, China). Sodium Citrate Antigenic Repair Solution (catalog number: AR0024) was purchased from BOSTER (CA, USA). CD31 (catalog number: ab28364), CD206 (catalog number: PA5-101657), KI67 (catalog number: ab16667), K6 (catalog number: bsm-60235R), CCR7 (catalog number: ab253187) were purchased from Abcam (Shanghai, China), LY6G (catalog number: 551459) was purchased from BD Pharming. DAB (catalog number: ZLI-9018) was purchased from ZSGB-BIO (Beijing, China). HRP-labeled Goat Anti-Rabbit IgG (H + L) (catalog number: A0208) was purchased from Beyotime (Shanghai, China). The rat 2-step kit (catalog number: PV-9004) was

purchased from ZSGB-BIO (Beijing, China).

2.2. Preparation of scaffold

To prepare the electrospinning solution, 20 g of polycaprolactone (PCL) and F127 were added to a 1:4 mixture of DCM/DMF and dissolved together. Nanofiber membranes with a thickness of about 500 μm were prepared using 25 ml of electrospinning solution. The spinning voltage was 18 kV. The distance between the high-speed rotating drum and the spinneret (22-gauge needle) was 18 cm. The syringe pump speed was 0.7 ml/h, and the hoop speed was 1800 rpm/m. The obtained nanofiber membrane was soaked in liquid nitrogen for 3 min and then cut into nanofiber strips. Weaving technology was used to weave the cut nanofiber strips into criss-crossing "bamboo basket" scaffolds. The scaffold edges were then sealed and fixed through cutting and heat treatment. The above "bamboo basket" scaffold was immersed in 1 M sodium borohydride solution for foaming and expansion treatment for 10 min. After close contact among the longitudinal and transverse fiber strips inside the stent, it was washed three times and freeze-dried with pure water.

2.3. Observation of micromorphology

After lyophilization, the 3D scaffold was immersed in pure water. After the fibers inside the scaffold were completely dispersed and stretched, they were placed in a −80 °C freezer until frozen, embedded using optimal cutting temperature compound (OCT), and ice cut by cryotome. Before observation, platinum was coated by ion sputtering (Hitachi S–3400 N, Japan) for 60 s. The front and cross-section of the 3D scaffolds were then observed using a scanning electron microscope (SEM, HITACHI SU8010, Japan) with an accelerating voltage of 10 kV.

2.4. Characterization of mechanical properties

The tensile properties of all samples were measured using an electronic universal material machine, including uniaxial aligned 3D nanofiber scaffolds, orthogonally woven 3D nanofiber scaffolds (3×3, 5×5, and 6×6 weaving scaffolds), cells infiltrated orthogonally woven scaffold after hernia repair. The length (4 cm), width (2 cm), and thickness (1 mm) of all samples were unified standards. A 100 N load cell was used to load samples at a tensile rate of 10 mm/min until the fiber broke. Finally, the maximum tensile stress, strain fracture rate, and Young's modulus were measured for all samples.

2.5. Bidirectional staining of fibers for FITC and Cy5

Firstly, 5 % FITC and 1 % Cy5 solutions were prepared and stored in a light-proof place for spare use. Then, the FITC and Cy5 solutions were added drop by drop (5μL/drop) to two different directions of the orthogonally woven scaffold. After freeze-drying overnight, the orthogonally woven scaffold loaded with different dyes was successfully prepared. Finally, the stained PCL fibers were subjected to confocal microscopy to capture fluorescence images.

2.6. Cytocompatibility of composite scaffold

8 PCL nanofiber strips with 3 vertical and horizontal strips were prepared by weaving and foaming them into a square nanofiber scaffold of 1.5 cm × 1.5 cm, soaked in 0.5 % gelatin for 2 h, and then frozen dry. Excess gelatin around the bracket was removed, and the scaffold was placed on an ultra-clean platform for 2 h under ultraviolet light. Then, 100 μl (1 million) of HUVECs cell suspension was added dropwise to the transverse PCL fiber strips, and 100 μl (1 million) of BMSCs cell suspension was added dropwise to the longitudinal PCL fiber strips. The scaffold with two types of cells was placed in a 37 °C 5 % CO2 incubator for 30 min, and then about 1.5 ml of complete medium was added to each scaffold after the cells were slowly attached. After the supplementation of the complete medium was completed, it was put back into the incubator for continued culturing, and the medium was changed once a day. On days 7 and 14, the 4 % paraformaldehyde was used to fix the scaffold, and the PBS was used to wash the scaffold 3 times. Then, the scaffold was imaged with a laser confocal scanning microscope (ZEISS Axio Vert.A1, Germany).

2.7. Growth factor loading

Eighteen pre-prepared orthogonally woven nanofiber scaffolds coated with GelMA and freeze-dried. Six scaffolds were selected for loading VEGF, and each scaffold was uniformly dropped with 200 μl of VEGF solution (200 ng/scaffold). Similarly, six scaffolds were chosen for loading bFGF, and each scaffold was uniformly dropped with 200 μl of bFGF solution (200 ng/scaffold). For the dual growth factor loaded scaffold, one direction of 3D PCL nanofibers was dropped with bFGF (100 ng), and another direction of 3D PCL nanofibers was dropped with VEGF (100 ng). Finally, the growth factor-loaded orthogonally woven nanofiber scaffolds were freeze-dried for subcutaneous implantation.

2.8. Subcutaneous implantation

Twelve SD female rats (6 weeks old, 200 g) were purchased from the animal experimental center of Wenzhou Institute, University of Chinese Academy of Sciences (WIUCAS23092105). All rats were divided into four groups: the control group, the bFGF group, the VEGF group, and the bFGF + VEGF group. Before surgery, the SD rats were anesthetized with isoflurane. After iodophor disinfection, a skin incision about 2 cm long was made on each back side. The distance between the bilateral back incisions was about 2–2.5 cm. Then, tissue forceps were used to separate the skin and the subcutaneous superficial fascia. 2 cm × 2 cm subcutaneous bags were made under the local skin. Finally, the 3D scaffolds of the same size and different components were implanted into the subcutaneous capsule according to the pre-grouping situation. After 7 d of implantation, the buried materials were taken from the planting position. After sampling, all rats were executed by anesthetic overdose. Local skin tissues continued to be dehydrated, paraffin-embedded, sectioned, and H&E stained for histological analysis to observe local vascularity and granulation tissue implantation.

## 2.9. Abdominal wall defect repair

Twelve SD female rats (8 weeks old, body mass of 220–260 g) were purchased from the animal platform of Wenzhou Institute, University of Chinese Academy of Sciences (WIUCAS23092105). A sufficient amount of 25 mm × 25 mm size and 5 mm height of PCL nanofiber woven patch material was prepared. SD rats were randomly divided into 2 groups. All SD rats were anesthetized with isoflurane. In the control group, a 25 × 25 mm defect was created in the center of the rats' abdominal wall. The patch material was then sutured to the tissue edge using surgical thread. The material was taken out for analysis after both 1 and 2 months. In the experimental group, the patch material was first buried in the superficial subcutaneous tissue of the abdomen, and a 25 × 25 mm abdominal wall tissue defect model was created in the middle of the abdominal wall after 2 weeks, the patch material that had grown into the tissue was flipped over to the site of the abdominal wall tissue defect, and the intersecting edges were closed with surgical suture. The material was taken out after both 1 month and 2 months. Intestinal adhesion and hernia repair of the two groups were compared by visual observation and Masson staining after sampling.

2.10. Diabetic skin wound healing

Forty-eight male ICR mice (8 weeks old, body mass of 35–40 g) were purchased from the animal platform of Wenzhou Institute, University of
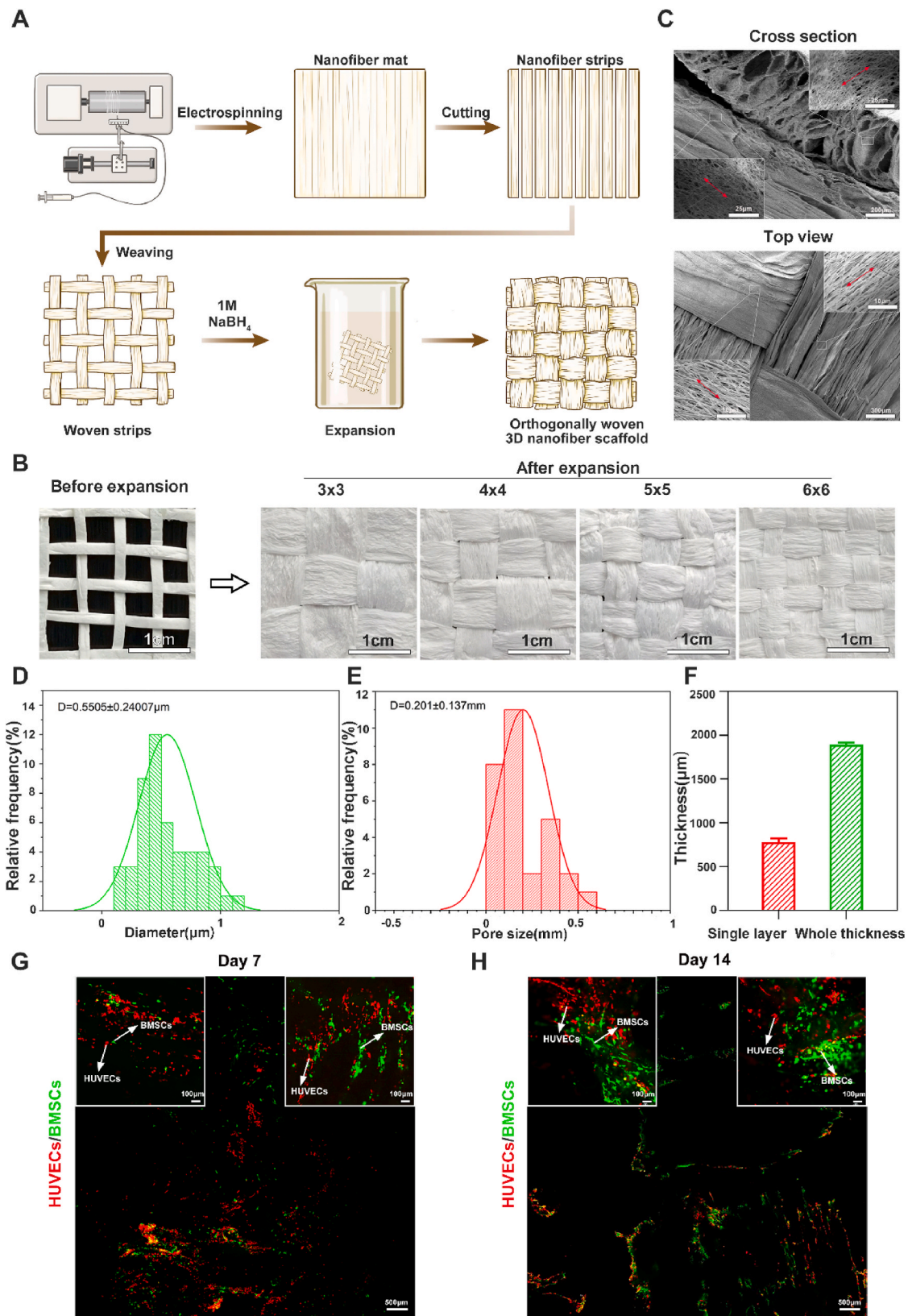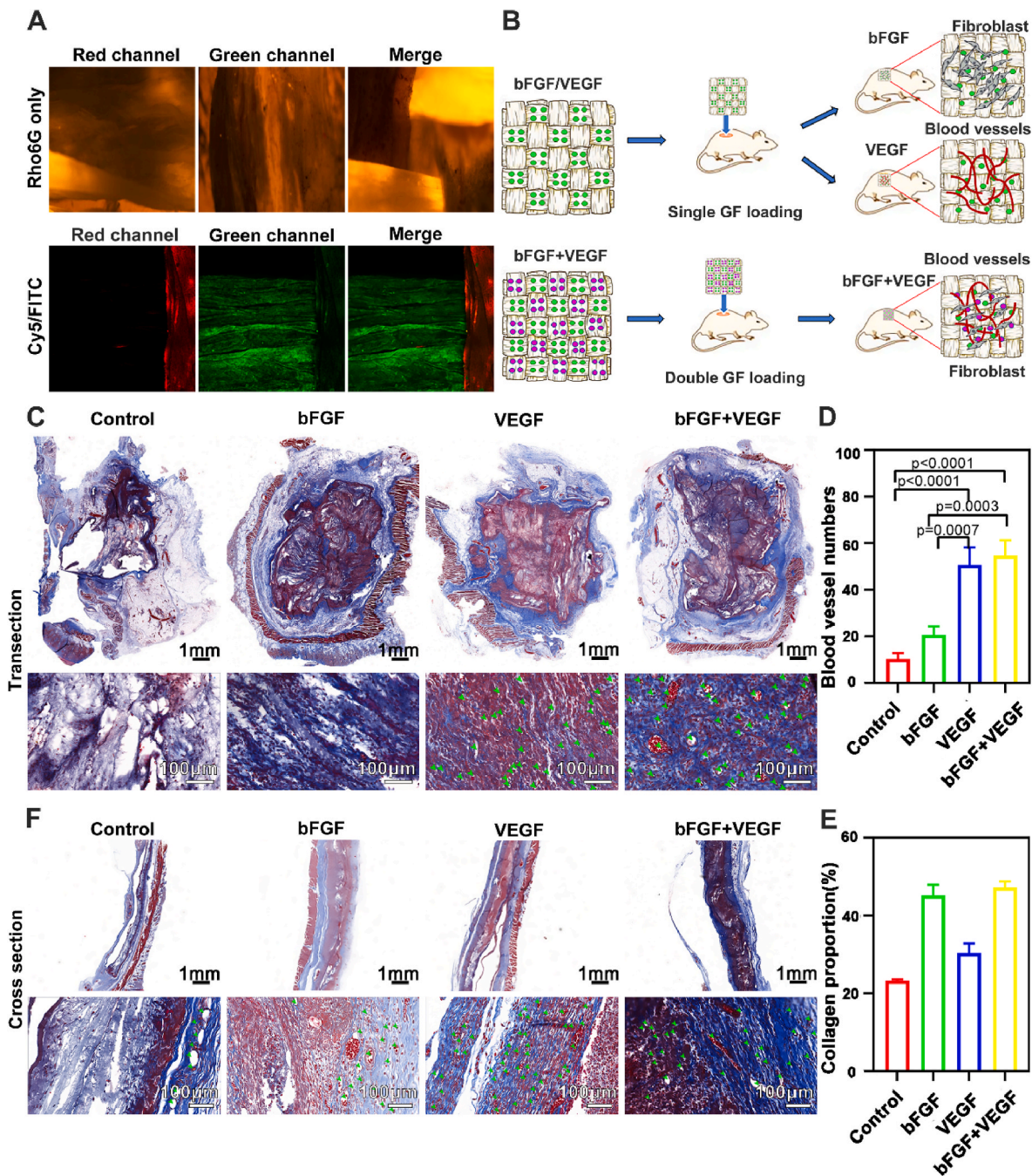
Fig. 2. The fabrication of an orthogonally woven 3D nanofiber scaffold. (A) The schematic illustrates the fabrication processes of an orthogonally woven 3D nanofiber scaffold containing electrospinning, cryo-cutting, weaving, and modified gas-foaming expansion. (B) The woven PCL nanofiber strips before expansion and the expanded orthogonally woven 3D nanofiber scaffold, the number of knitted strips could be adjustable. (C) The cross-section and top view of the orthogonally woven 3D nanofiber scaffold. (D) The nanofiber diameter quantification of the orthogonally woven 3D nanofiber scaffold. (E) The inner pore size of the orthogonally woven 3D nanofiber scaffold. (F) The thickness of one layer and the whole scaffold. (G) The proliferation and interaction between BMSCs and HUVECs after 7 days of co-culture. (H) The proliferation and interaction between BMSCs and HUVECs after 14 days of co-culture.
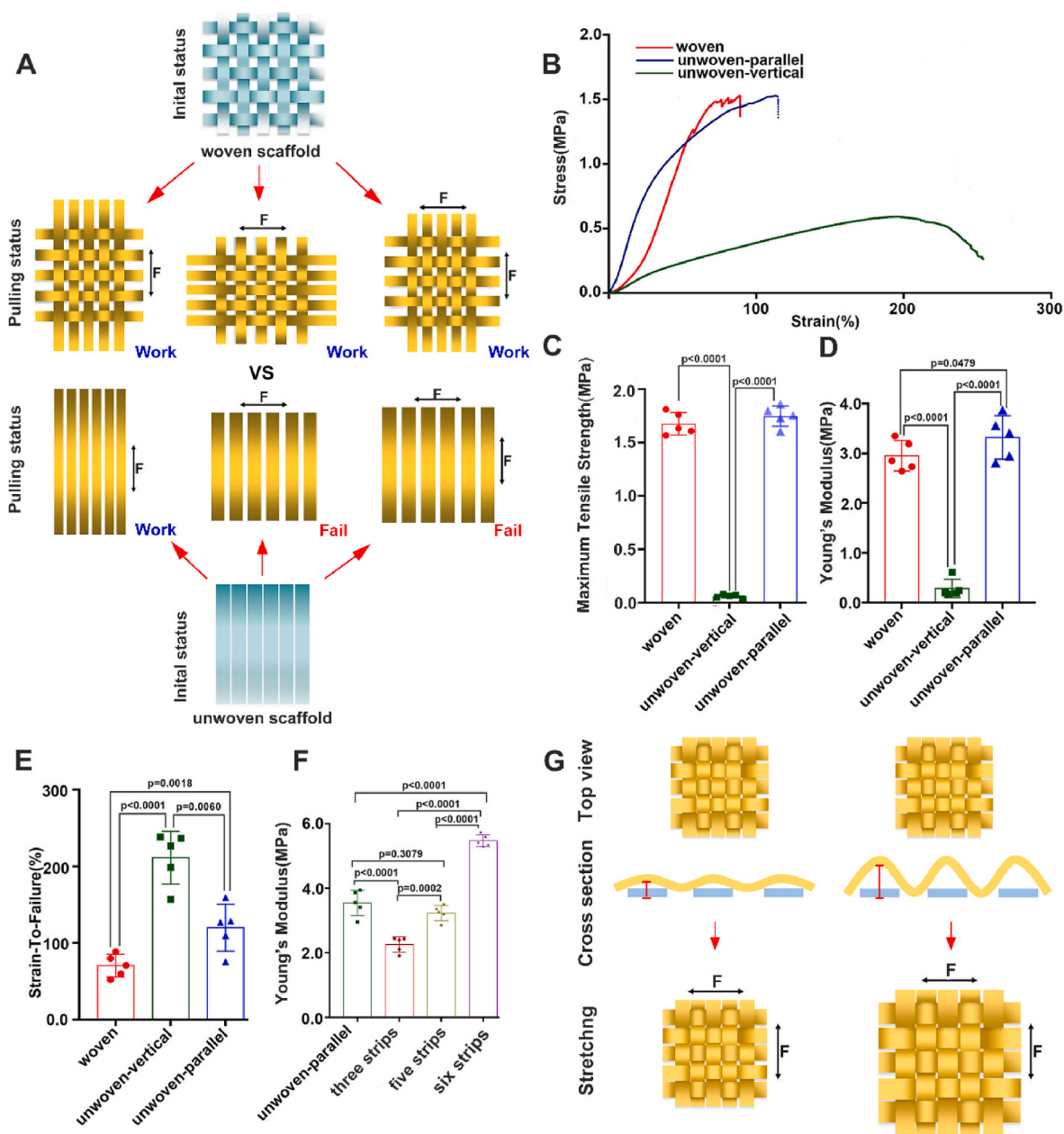
Fig. 3. The mechanical properties of orthogonally woven 3D nanofiber scaffold. (A) The schematic illustrates the situation of the orthogonally woven 3D nanofiber scaffold under stretching compared to the uniaxial aligned 3D nanofiber scaffold. (B) The stress-strain curve of the orthogonally woven 3D nanofiber scaffold and uniaxial aligned 3D nanofiber scaffold in two different directions. (C, D) The maximum tensile strength and Young's modulus of the orthogonally woven 3D nanofiber scaffold and uniaxial aligned 3D nanofiber scaffold in two different directions. (E) The breaking strain of the orthogonally woven 3D nanofiber scaffold and uniaxial aligned 3D nanofiber scaffold in two different directions. (F) The Young's modulus of uniaxial aligned 3D nanofiber scaffold and the orthogonally woven 3D nanofiber scaffold with 3×3, 5×5, and 6×6 strips. (G) The schematic illustrates the stain of the orthogonally woven 3D nanofiber scaffold could be adjusted by increasing the wavelength of expanded strips.

Chinese Academy of Sciences. The number of animal experimental ethical inspection is WIUCAS23092202. A murine model of type II diabetes mellitus was prepared by intraperitoneal injection of streptozotocin (STZ) (50 mg/kg), with a one-day interval between each injection and five consecutive injections, followed by two weeks of continuous blood glucose monitoring using a glucometer (Roche Diagnostics, Shanghai, China). Diabetes mellitus was considered to be present if the whole blood glucose level exceeded 19 mmol/l and was accompanied by symptoms such as weight loss, excessive drinking, urination, and increased appetite. Sufficient amounts of PCL nanofiber scaffolds, PELNAC material (commercial), and Lando material (commercial) were prepared. All materials were 8 mm in diameter and 5 mm

in thickness. The ICR mice were divided into 4 groups according to the materials used. They were the control group, PCL nanofiber scaffold group, PELNAC group, and Lando group. The materials were taken at 3, 7, 14, and 21 d, respectively. After the ICR mice were anesthetized by inhalation of isoflurane, a symmetrical 8-mm-diameter wound model was created on the back of the mice. The edges of the wound were sutured with rubber pads to slow down the contraction of trauma healing. Different material scaffolds were placed on the wound and then applied with a 3 M transparent dressing. At the end of sampling, all mice died of an anesthetic overdose. Samples containing healthy skin tissues from the trauma site and surrounding areas were used for subsequent histological and RNA-seq analyses.

Fig. 4. The drug loading of the orthogonally woven 3D nanofiber scaffold. (A) The demonstration of one drug loading in the whole orthogonally woven 3D nanofiber scaffold, and two drug loading in two different directions of the scaffold. (B) The schematic illustrates a single bFGF or VEGF loading and both bFGF and VEGF loading in the orthogonally woven 3D nanofiber scaffold. (C) The transection trichrome staining of the scaffold only, bFGF loaded scaffold, VEGF loaded scaffold, and bFGF/VEGF co-loaded scaffold with surrounding tissues after subcutaneous implantation for 1 week. (D) The quantification of newly formed blood vessels among the four groups after subcutaneous implantation for 1 week. (E) The quantification of collagen deposition among the four groups after subcutaneous implantation for 1 week. (F) The cross-section trichrome staining shows the scaffold only, bFGF loaded scaffold, VEGF loaded scaffold, and bFGF/VEGF co-loaded scaffold with surrounding tissues after subcutaneous implantation for 1 week. The green arrows indicate the newly formed blood vessels.

2.11. Histological observations

After 3, 7, 14, and 21 d of treatment, the samples containing the wound area and surrounding healthy skin tissue were placed in 4 % paraformaldehyde for 1 d for subsequent dehydration, paraffin embedding, and sectioning (5 μm). The cut tissues were baked for 2 h and then de-waxed with xylene. Subsequently, HE staining was used to observe the cellular infiltration from the peripheral tissues to the center of the wound. Masson staining was used to analyze new collagen and blood vessels in the wound site.

2.12. Immunohistochemical staining

Paraffin sections of 5 μm thickness were deparaffinized, heated in citrate buffer to retrieve the antigen, and then treated with 3 % H_2O_2 for 15 min to inactivate the endogenous peroxidase activity. Then they were blocked with goat serum and BSA solution for 1 h and incubated with primary antibodies (CD31:1/200; CD206:1/300; CCR7:1/300; LY6G: 1/

200; K6:1/200; KI67:1/200) at 4 °C overnight. Then, it was followed with the corresponding secondary antibodies. After diaminobenzidine (DAB) color development, tissue sections were stained and observed under a microscope. Image Pro Plus software was used to quantify the proportion of positively stained cells in each field of view.

2.13. RNAseq and bioinformatics analysis

Tissue samples were taken from 7d wounds of diabetic mice in PCL and Pelnac groups and sent to Shanghai Ouyi Biomedical Technology Co. Total RNA was extracted using TRIzol reagent. RNA purity and quantification were determined using a NanoDrop 2000 spectrophotometer (Thermo Scientific, USA). RNA integrity was assessed using an Agilent 2100 Bioanalyzer (Agilent Technologies, Santa Clara, CA, USA). Transcriptome libraries were constructed using the VAHTS Universal V6 RNA-seq Library Prep kit. Transcriptome sequencing and analysis were performed. Differentially expressed genes were screened using DESeq2 software. Genes that met the threshold of q value < 0.05 and |Foldchange| > 2 were defined as differentially expressed genes. Subsequently, GO, KEGG Pathway, and other enrichment analyses were performed on the differentially expressed genes based on the hypergeometric distribution algorithm to filter out the significantly enriched functional entries.

2.14. Statistical analysis

The data were presented as means $\pm$ standard errors of the means. Differences among different groups were assessed using one-way ANOVA followed by post hoc tests. The value of $p < 0.05$ was considered statistically significant.

3. Results and discussion

3.1. Fabrication and characterization of orthogonally woven 3D nanofiber scaffolds

Orthogonally woven 3D nanofiber scaffolds were obtained by transforming 2D electrospun nanofiber mats following our established protocols. Fig. 2A schematically illustrates the process of preparing the orthogonally woven 3D nanofiber scaffolds. Briefly, the nanofiber mat with a thickness of about 500 μm was soaked in liquid nitrogen for 3 min and then cut into nanofiber strips, and weave the cut nanofiber strips into criss-crossing "bamboo basket" scaffolds. Following, the knitted nanofiber strips were immersed in a sodium borohydride solution for foaming until the longitudinal and transversal fiber strips were in close contact. Finally, the expanded orthogonally woven 3D nanofiber scaffolds were freeze-dried, the edges were thermo-fixed, and the whole scaffold was washed and freeze-dried again for future use. The weaved strips show a loose structure, whereas expanded orthogonally woven 3D nanofiber scaffolds are more compact after the foaming treatment (Fig. 2B). The number of strips within the scaffold could be adjustable from 2×2 to 6×6 in the area of 6.25 cm² (2.5cm × 2.5 cm). In Fig. 2C, the SEM images show a porous structure inside the scaffold. The top view shows a parallel-arranged channel structure on the surface of the scaffold, and these channels consist of uniaxial aligned nanofibers (insert images). The average diameter of the fibers is statistically calculated to be 0.55 ± 0.24 μm (Fig. 2D). The average pore size of the scaffold is 0.2 ± 0.14 mm (Fig. 2E). The whole thickness of the scaffold is 1.79 ± 0.02 mm, and the single layer of the scaffold is 781.00 ± 41.86 μm (Fig. 2F).

To verify the cytocompatibility of the orthogonally woven 3D nanofiber scaffolds, the human umbilical vein endothelial cells (HUVECs) and bone marrow mesenchymal stem cells (BMSCs) were seeded in different directions of expanded nanofiber strips of the orthogonally woven 3D nanofiber scaffold. After 7 days of culture, HUVECs and BMSCs were attached well to the surface (Fig. S1) and

started to contact each other (Fig. 2G). The cell density of HUVECs and BMSCs was significantly increased after 14 days of culture (Fig. 2H and Fig. S2).

3.2. Characterization of the mechanical properties of the orthogonally woven 3D nanofiber scaffolds

As shown in Fig. 3A, the schematic illustrates that the orthogonally woven 3D nanofiber scaffold can withstand forces in both directions while maintaining structural integrity. In comparison, the uniaxially aligned 3D nanofiber scaffold can only bear the force in the direction of nanofibers. Tensile tests were performed to study the mechanical properties of the orthogonally woven 3D nanofiber scaffold and uniaxial aligned 3D nanofiber scaffold (Fig. 3B). In the orthogonally woven 3D nanofiber scaffold, the stain-stress curves of two directions are similar (Fig. S3), the tensile strength could reach 1.528 MPa (88.710 % stain) because of uniform weaving. In the uniaxial aligned 3D nanofiber scaffold, only the direction parallel to the nanofibers has specific tensile properties. The tensile strength was 1.531 MPa (118.3999 % stain) close to the weaved scaffold. While in the direction perpendicular to the nanofibers, the tensile strength was only 0.503 MPa (229.419 % strain) (Fig. 3C). The corresponding Young's modulus was 2.952 ± 0.305 MPa (woven), 0.282 ± 0.185 MPa (unwoven-vertical) 3.546 ± 0.398 MPa (unwoven-parallel) (Fig. 3D). In addition, the strains at break were 211.439 ± 34.430 % (unwoven-vertical), 146.674 ± 26.850 % (unwoven-parallel), 80.328 ± 14.713 % (woven) (Fig. 3E). To match the mechanical properties of different soft tissues, the mechanical properties of the orthogonally woven 3D nanofiber scaffold can be changed according to the actual application requirements by increasing or reducing the number of PCL nanofiber strips. As shown in Fig. 3F, the Young's modulus of the scaffold increased from a 3×3 weaving style to a 6×6 weaving style. Moreover, the scaffold requires greater flexibility in areas with large deformations, such as joints. This goal can be achieved by increasing the "wavelength" of the strip (Fig. 3G).

3.3. Drug loading of the orthogonally woven 3D nanofiber scaffold

Firstly, we used dyes to simulate drug loading into the orthogonally woven 3D nanofiber scaffold. As shown in Fig. 4A, for one thing, the whole orthogonally woven scaffold could be loaded with the same drug (Rhodamine 6G). For another, two directions of the orthogonally woven 3D nanofiber scaffold could be loaded with two different drugs (Cy5 and FITC). The drug loading method can be encapsulation or simple physical absorption (Fig. S4). Then, we tried to co-load the bFGF and VEGF into the orthogonally woven 3D nanofiber scaffold to promote the migration of fibroblasts and endothelial cells (Fig. 4B). The bFGF was loaded in one direction of the scaffold, and the VEGF was loaded in the other direction. The subcutaneous implantation of growth factor-loaded orthogonally woven 3D nanofiber scaffold was used to evaluate its potential for soft tissue regeneration. In comparison between groups (Fig. 4C), we found that significant cell infiltration and collagen deposition were observed in the bFGF-loaded scaffold compared to the control group after 1 week of implantation. Obvious blood vessel formation was observed in the VEGF-loaded scaffold compared to the bFGF-loaded scaffold, representing a critical physiological and pathological neovascularization regulatory system. Similar cell infiltration, collagen deposition, and new blood vessel formation were observed in both bFGF and VEGF co-loaded scaffolds after 1 week of implantation. The quantitative analysis further verified the addition of VEGF could promote angiogenesis (Fig. 4D), and the addition of bFGF could accelerate collagen deposition (Fig. 4E). The cross-section trichrome staining results of the four groups after subcutaneous implantation (Fig. 4F) were consistent with the transection trichrome staining results (Fig. 4C).
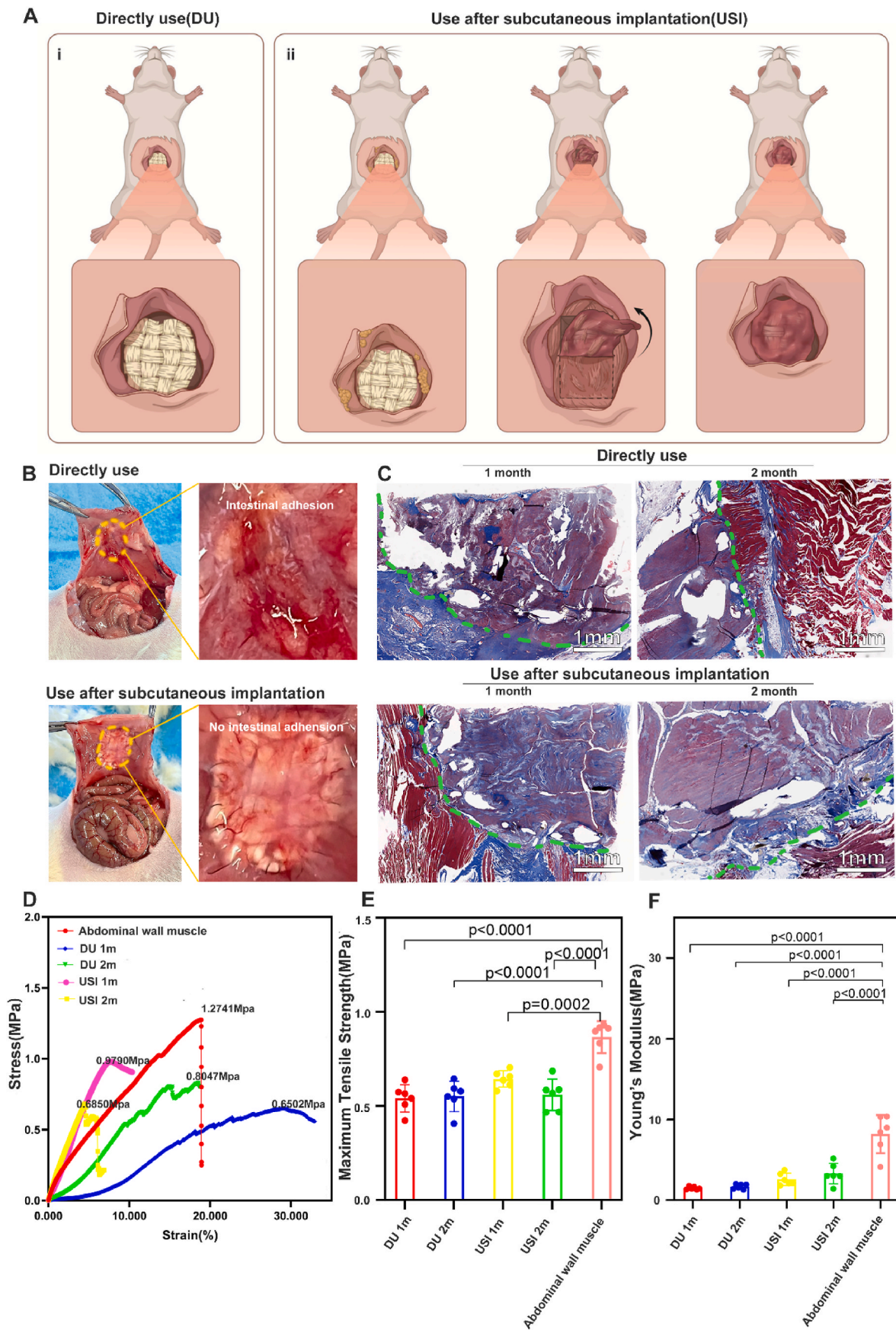
Fig. 5. The application of orthogonally woven 3D nanofiber scaffold in hernia repair. (A) The schematic illustrates the application of an orthogonally woven 3D nanofiber scaffold in hernia repair. Two methods were used in this study. One method was directly used (DU), and another was subcutaneously implanted for 2 weeks, then cut three sides of the scaffold and flipped horizontally to the hernia area. (B) The photographs of the repaired hernia were treated with scaffold directly for 2 months, or subcutaneously implantation for 2 weeks first and then applied in the hernia area for 2 months. (C) The trichrome staining of regenerated hernia tissue was treated with scaffolds directly for 1, 2 months, or subcutaneously implantation of scaffolds for 2 weeks first and then applied in the hernia area for 1, 2 months. (D) The strain-stress curve of regenerated hernia tissue was treated with scaffolds directly for 1, 2 months, or subcutaneously implantation of scaffolds for 2 weeks first and then applied in the hernia area for 1, 2 months. (E, F) The maximum tensile strength and Young's modulus of the regenerated hernia tissue that treated with scaffolds directly for 1, 2 months, or subcutaneously implanted scaffolds for 2 weeks first and then applied in the hernia area for 1, 2 months.

3.4. In vivo hernia repair

The orthogonally woven 3D nanofiber scaffolds mimic the abdominal muscle tissue of biaxially aligned muscle fibers. Therefore, we first explored the role of orthogonally woven 3D nanofiber scaffolds in hernia repair. The study used the orthogonally woven 3D nanofiber scaffold in two different methods. One approach is to suture the scaffold directly to the defect area (Fig. 5Ai), and another method is to do a subcutaneous implantation for 2 weeks before using it (Fig. 5Aii). After 1 and 2 months of implantation (Fig. 5B and Fig. S5), intestinal adhesions occurred in the DU group (direct use), a common complication of hernia repair. By comparison, the inner wall of the abdominal cavity was smooth and there was no intestinal adhesion problem in the USI group (use after subcutaneous implantation). Suggesting the orthogonally woven 3D nanofiber scaffolds for use after subcutaneous implantation may be preferable to direct use. The trichrome staining further revealed a good integration at the junction between the scaffold and abdominal wall muscle (Fig. 5C). The tensile test of the regenerated area showed that Young's modulus of the USI group is closest to Young's modulus of normal abdominal wall muscle tissue (Fig. 5D and F). Moreover, the DU and USI groups could recover about 63 % and 80 % of the tensile strength of the abdominal wall muscle (Fig. 5E).

3.5. In vivo diabetic skin wound healing

The orthogonally woven 3D nanofiber scaffold can recruit cells from four directions. Thus, it has the potential to be used for skin wound healing. To verify the effects of the orthogonally woven 3D nanofiber scaffold on skin wound healing, the anti-contraction diabetic skin wound healing model was established, and the commercial products Lando and PELNAC were used as positive controls. As shown in Fig. 6A-C, the residual wound size of the orthogonally woven 3D PCL nanofiber scaffold (PCL) group was significantly decreased compared to the other three groups. On day 7, the wound size of the PCL group was 42.990 %, whereas the wounds in the other groups remained larger, with sizes of 76.960 % (control group), 53.200 % (Lando group), and 52.600 % (PELNAC group), respectively. In addition, the PCL group first achieved wound healing on day 14. After 21 days, the wounds of the PCL group exhibited the smallest scar area (4.670 %), whereas in the other groups, the scar sizes were 8.820 % (control group), 9.870 % (Lando group), and 9.370 % (PELNAC group).

The histological observations further revealed the proliferative responses of wound areas in the PCL group are relatively strong. More granulation tissue formation of PCL scaffold-treated wound bed was observed when compared to control, Lando, and PELNAC groups after 3 and 7 days of treatment (Fig. 6D). The trichrome staining discovered that more collagen deposition was found in the PCL groups compared to the other three groups at the early stage of wound healing (day 3 and day 7) (Fig. 6F and Figs. S6C and S6D). Within the newly formed granulation tissues, the expression of Ki67 (a marker for cell proliferation) of the PCL group was significantly higher than the control, Lando, and PELNAC groups after 7 and 14 days of treatment (Figs. S7A and S7B). There was no difference in the expression of CD31 among the PCL, Lando, and PELNAC groups after 7 and 14 days of treatment (Figs. S7C and S7D). In addition, we also examined the proliferative reaction of the epidermis. The expression of Keratin 6 (K6) in the regenerated epidermis of the PCL group was increased compared to the control, Lando, and PELNAC

groups after 7 and 14 days of treatment (Figs. S7E and S7F). After 14 days of treatment, the PCL group had completed re-epithelialization, while there was also a small gap that was not covered by the epidermis in the Lando and PELNAC groups, especially in the control group. After wound healing, there were more new hair follicles in the wound center area of the PCL group compared to the control, Lando, and PELNAC groups on day 21 (Figs. S6A and S6B), and the histomorphology of PCL scaffold regenerated tissue is closer to healthy skin. The re-epithelialization rate further verified the histological observations (Fig. 6E). The histological observations have clearly exhibited that the orthogonally woven 3D nanofiber scaffold could promote granulation tissue formation, collagen deposition and re-epithelialization.

3.6. Pro-healing mechanism of orthogonally woven 3D nanofiber scaffold

A non-targeted RNA-seq was performed to explore the potential pro-healing mechanism of an orthogonally woven 3D nanofiber scaffold compared to PELNAC based on the wound healing results. As shown in Fig. 7A, the differentially expressed genes were related to cell movement, proliferation, extracellular matrix deposition, and inflammatory and immune responses. The above results have verified the activities of cell movement, proliferation, and extracellular matrix deposition in the orthogonally woven 3D nanofiber scaffold-treated group. Among these differential genes, most were associated with inflammation and immune response (Fig. 7A). The GO functional enrichment further discovered that these differentially expressed genes regulated the chemotaxis of monocytes, lymphocytes, and neutrophils (Fig. 7B). To verify the bioinformatics results, the immunohistochemical staining of inflammatory cells (*e.g.*, macrophage, monocytes, granulocytes, and neutrophils) in the wound area of the PCL nanofiber treated group at an early stage of wound healing were performed. As shown in Fig. 7C and D, the expression of CCR7 (M1 type macrophage) in the PCL-treated group was significantly lower than in the control, Lando, and PELNAC groups on both day 3 and day 7. On the contrary, CD206 (M2 type macrophage) expression in the PCL-treated group increased compared to the control, Lando, and PELNAC groups on day 3 and day 7 (Fig. 7E and F). And the ratio of M2 macrophage numbers/M1 macrophage numbers was greater than 5 on day 3 and greater than 10 on day 7 (Fig. 7G), which belonged to a pro-regenerative inflammatory status. In addition, the expression of LY6G (a pan marker of monocytes, granulocytes, and neutrophils) in the wound area of PCL- and PELNAC-treated groups was obviously lower than control and Lando groups on both day 3 and day 7 (Fig. 7H and I). Moreover, the KEGG enrichment discovered potential signaling pathways that regulate inflammatory responses, including the IL-17 signaling pathway, NF-kappa B, and NF-kappa B signaling pathway (Fig. S8).

4. Discussion

In the presented study, we developed an orthogonally woven 3D nanofiber scaffold using electrospinning, weaving and modified gas-foaming technology. The fabricated orthogonally woven 3D nanofiber scaffold has a porous internal structure and bidirectionally parallel-arranged nanofibers. Compared with other in vitro models (*e.g.*, hydrogels [17], 3D printed scaffold [18]), our 3D nanofiber scaffold is closer to the 3D microenvironment of the human extracellular matrix [12,19]. In vitro, it is a good platform for exploring the interactions
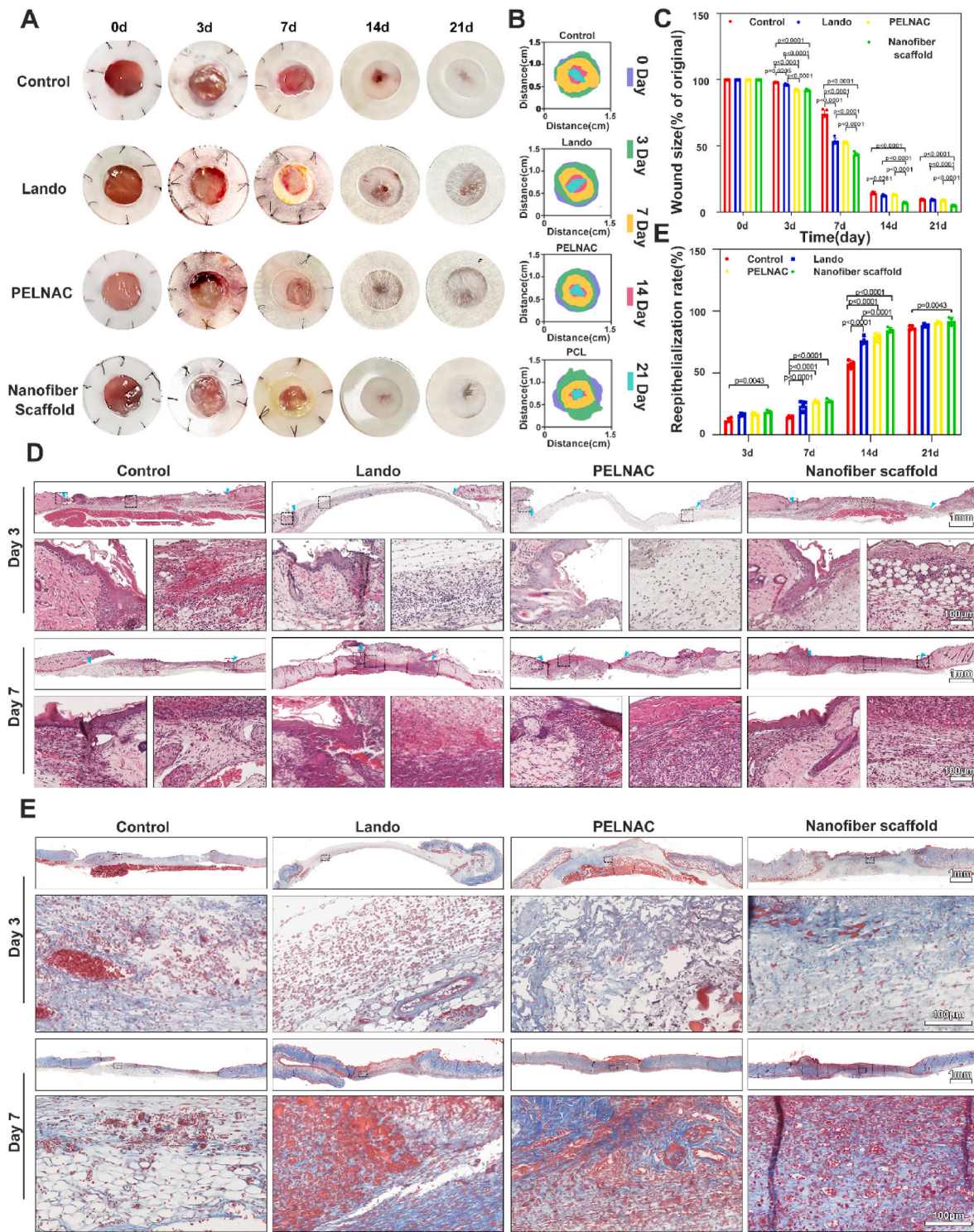
Fig. 6. The effects of orthogonally woven 3D nanofiber scaffold on skin wound healing. (A) Photographs of chronic skin wounds treated with Lando, PELNAC, PCL orthogonally woven 3D nanofiber scaffold (PCL), the wounds without any treatment as the Control group after 3, 7, 14, and 21 days, respectively. (B) The changes in wound size of control, Lando, PELNAC, and PCL groups from day 0 to day 21. (C) The wound closure rate of the Control, Lando, PELNAC, and PCL groups at each indicated time point. (D) The histological observations of wound area in the Control, Lando, PELNAC, and PCL groups on day 3 and 7 days, respectively. (E) The wound re-epithelialization rate of the Control, Lando, PELNAC, and PCL groups on day 3, 7, 14, and 21 days, respectively. (F) The trichrome staining of the wound area in the Control, Lando, PELNAC, and PCL groups after 3 and 7 days of treatment.

between various cells because of its structural heterogeneity [20]. In vivo, it can recruit many cells from the surroundings in a short time to participate in and accelerate tissue repair. Besides structure heterogeneity, another advantage is its orthogonally woven mechanical properties in two directions. It has tensile properties in two directions, giving it

more advantages as a patch scaffold to meet the soft tissue repair needs of stressed and movable parts [21]. In addition, different soft tissues of the human body have different mechanical properties. For example, muscle tissue has stronger mechanical properties than skin tissue [22]. To match the mechanical properties of various soft tissues, the

(caption on next page)
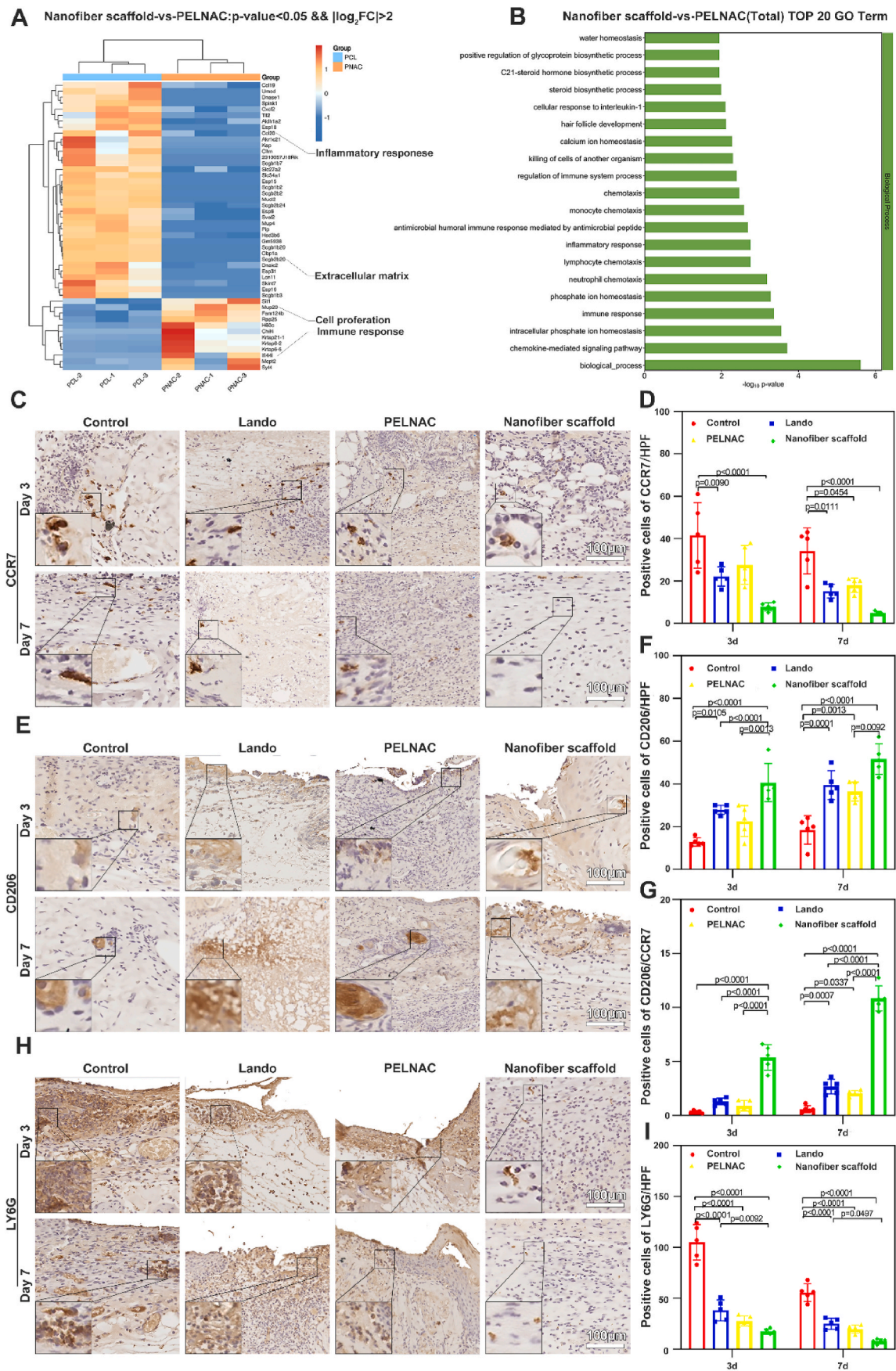
Fig. 7. The potential pro-healing mechanism of orthogonally woven 3D nanofiber scaffold. (A) The heatmap exhibits the differentially expressed genes in the PCL nanofiber scaffold-treated wounds compared to PELNAC-treated wounds. (B) The GO functional enrichment of these differentially expressed genes. (C) Immuno-histochemical staining of CCR7 in wound center area of the Control, Lando, PELNAC, and PCL groups after 3 and 7 days of treatment. (D, F) The quantification of CCR7 (M1 macrophage) and CD206 (M2 macrophage) positive cells in the wound center area of the Control, Lando, PELNAC, and PCL groups after 3 and 7 days of treatment. (E) Immunohistochemical staining of CD206 in wound center area of the Control, Lando, PELNAC, and PCL groups after 3 and 7 days of treatment. (G) The ratio between the numbers of M2 type macrophage and M1 type macrophage of the Control, Lando, PELNAC, and PCL groups on day 3 and day 7. (H) Immuno-histochemical staining of LY6G in wound center area of the Control, Lando, PELNAC, and PCL groups after 3 and 7 days of treatment. (I) The quantification of LY6G (a pan marker of monocytes, granulocytes, and neutrophils) positive cells in the wound center area of the Control, Lando, PELNAC, and PCL groups after 3 and 7 days of treatment.

mechanical properties of the orthogonally woven 3D nanofiber scaffold can be changed according to the actual application requirements by increasing or reducing the number of PCL nanofiber strips. This study used 2 × 2 and 3 × 3 woven nanofiber scaffolds for diabetic wound healing and abdominal wall defect repair. Because abdominal wall defects require stronger mechanical support. Moreover, it can also be further optimized by adding elastic polymer or stiff polymer (e.g., biodegradable polyurethane, polylactic acid, poly (lactic-co-glycolic acid)) to meet the requirements of different tissue regeneration [23,24].

For orthogonally woven tissue regeneration, we first explored its application in hernia repair and achieved promising results. In addition to hernia repair, our scaffold material shows promise for repairing gynecological pelvic organ prolapse. Previously, polypropylene mesh was the most common type of pelvic prolapse patch used in gynecology [25]. However, it has many side effects and is banned by the FDA. The current alternative material, acellular dermal matrix, degrades quickly and is very expensive [26,27]. By comparison, our orthogonally woven 3D nanofiber scaffold has strong tissue compatibility, the degradation time matches the pelvic repair time, and there will be no side effects such as displacement and perforation of the vaginal wall after transplantation in vivo [25,28]. What's more, the degradation time of PCL is 1–2 years, which is consistent with the pelvic floor reconstruction time. The degradation time of our orthogonally woven scaffold is significantly longer than that of allogeneic decellularized scaffolds and xenogeneic decellularized scaffolds.

For diabetic skin wound healing, the histological observations have clearly exhibited that the orthogonally woven 3D nanofiber scaffold could promote granulation tissue formation, collagen deposition, and re-epithelialization. We speculate that this is mainly due to the ability of oriented nanofibers to encourage the migration of fibroblasts and keratinocytes from surrounding healthy tissue to the wound area [29]. Because aligned architectures provide contact guidance cues that direct focal adhesion maturation and associated F-actin alignment in a constrained manner [30]. The mouse wound model cannot reflect the role of an orthogonally woven scaffold in deep ulcer wound repair. The thickness of the orthogonally woven scaffold can be customized according to the depth of the wound [31]. Based on the wound assessment results, thicker scaffolds can be selected for deep wounds, and thinner scaffolds can be used for superficial wounds.

Interestingly, we found that orthogonally woven 3D nanofiber scaffolds can recruit not only fibroblasts, keratinocytes, and endothelial cells but also immune cells to regulate the local inflammatory microenvironment of the wound. Monocytes and neutrophils are the primary inflammatory cells in the early stages of wounds [32], and then monocytes alter their phenotype to become macrophages later [33]. In our study, the orthogonally woven 3D nanofiber scaffolds could promote monocyte and neutrophil infiltration (higher LY6G expression) because of the chemotactic induction of aligned nanotopographic cues. Together, the infiltrated neutrophils, monocytes, and macrophages facilitate debridement [34], providing a clean wound bed for granulation tissue formation. In addition, the local inflammatory state of the wound changes from pro-inflammatory to pro-regenerative level, suggesting the large number of inflammatory cells recruited in the early stage did not impair the wound healing process. Moreover, the polarization of M2 macrophages can further promote wound repair [35,36].

5. Conclusion

In this study, we prepared 3D PCL nanofiber scaffolds with a bamboo basket-like structure exhibiting excellent tensile properties. The bi-directionally aligned scaffolds recruited cells rapidly to infiltrate the material and secrete extracellular matrix, promoting granulation tissue formation. As a biopatch, the scaffold's flexibility enables adaptation to biological movements. Implantation in a full abdominal wall defect model demonstrated that the extensive granulation tissue formation beneath the skin could promote recovery of deep abdominal wall defects while reducing intestinal adhesion. As a dressing for chronic wounds, this skin scaffold can promote cell migration, production of value-added extracellular matrix, and secretion to accelerate healing. We demonstrated that the bi-directionally aligned scaffolds can also be loaded with single cells, multiple cells, or other drugs to aid functional recovery. The scaffold simultaneously enables the targeted delivery of two growth factors to spur collagen infiltration and angiogenesis. Therefore, the biaxially aligned PCL nanofiber scaffolds woven into strips exhibit great potential for repairing full-layer abdominal wall defects, healing chronic wounds, and enabling further targeted drug delivery applications.

Ethics approval and consent to participate

The subcutaneous implantation and abdominal wall defect repair experiments were approved by the animal experimental center of Wenzhou Institute, University of Chinese Academy of Sciences (**WIU-CAS23092105**). The diabetic skin wound healing experiment was approved by the animal experimental center of Wenzhou Institute, University of Chinese Academy of Sciences (**WIUCAS23092202**).

Funding

CRediT authorship contribution statement

Jiayi Yuan: Methodology, Investigation, Formal analysis. **Bingbing Sun:** Investigation, Formal analysis, Data curation. **Weixing Ma:** Resources, Project administration. **Chao Cai:** Writing – original draft, Investigation, Formal analysis. **Zhenzhen Huang:** Resources, Methodology, Investigation. **Peiyi Zhou:** Formal analysis, Data curation. **Lei Yi:** Visualization, Validation, Supervision, Software, Resources. **Lubin Liu:** Supervision, Resources, Project administration. **Shixuan Chen:** Writing – review & editing, Writing – original draft, Project administration.

Declaration of competing interest

All authors declare no conflicts of interest in this work, and all authors have read and agreed to this submission.

Acknowledgements

Appendix A. Supplementary data

Supplementary data to this article can be found online at https://doi.org/10.1016/j.bioactmat.2024.04.025.

References

[1] R. Wong, S. Geyer, W. Weninger, J.-C. Guimberteau, J.K. Wong, The dynamic anatomy and patterning of skin, Exp. Dermatol. 25 (2) (2016) 92–98.

[2] D.R. Smith, D.A. Caban-Rivera, M.D.J. McGarry, L.T. Williams, G. McIlvain, R. J. Okamoto, E.E.W. Van Houten, P.V. Bayly, K.D. Paulsen, C.L. Johnson, Anisotropic mechanical properties in the healthy human brain estimated with multi-excitation transversely isotropic MR elastography, Brain Multiphysics 3 (2022) 100051.

[3] Z. Liu, Z. Zhang, R.O. Ritchie, Structural orientation and anisotropy in biological materials: functional designs and mechanics, Adv. Funct. Mater. 30 (10) (2020) 1908121.

[4] A. Chanda, C. Callaway, Tissue anisotropy modeling using soft composite materials, Appl. Bionics Biomech. (2018), 2018.

[5] L. Astruc, M. De Meulaere, J.F. Witz, V. Nováček, F. Turquier, T. Hoc, M. Brieu, Characterization of the anisotropic mechanical behavior of human abdominal wall connective tissues, J. Mech. Behav. Biomed. Mater. 82 (2018) 45–50.

[6] N. Khuu, S. Kheiri, E. Kumacheva, Structurally anisotropic hydrogels for tissue engineering, Trends Chem. 3 (12) (2021) 1002–1026.

[7] X. Wang, J. Fang, W. Zhu, C. Zhong, D. Ye, M. Zhu, X. Lu, Y. Zhao, F. Ren, Bioinspired highly anisotropic, ultrastrong and stiff, and osteoconductive mineralized wood hydrogel composites for bone repair, Adv. Funct. Mater. 31 (20) (2021) 2010068.

[8] J. Xing, N. Liu, N. Xu, W. Chen, D. Xing, Engineering complex anisotropic scaffolds beyond simply uniaxial alignment for tissue engineering, Adv. Funct. Mater. 32 (15) (2022) 2110676.

[9] F.T. Moutos, L.E. Freed, F. Guilak, A biomimetic three-dimensional woven composite scaffold for functional tissue engineering of cartilage, Nat. Mater. 6 (2) (2007) 162–167.

[10] Q. Chen, J.D. Mangadlao, J. Wallat, A. De Leon, J.K. Pokorski, R.C. Advincula, 3D printing biocompatible polyurethane/poly(lactic acid)/graphene oxide nanocomposites: anisotropic properties, ACS Appl. Mater. Interfaces 9 (4) (2017) 4015–4023.

[11] J. Xie, B. Ma, P.L. Michael, Fabrication of novel 3D nanofiber scaffolds with anisotropic property and regular pores and their potential applications, Adv. Healthcare Mater. 1 (5) (2012) 674–678.

[12] S. Chen, A. McCarthy, J.V. John, Y. Su, J. Xie, Converting 2D nanofiber membranes to 3D hierarchical assemblies with structural and compositional gradients regulates cell behavior, Adv. Mater. 32 (43) (2020) 2003754.

[13] J. Jiang, S. Chen, H. Wang, M.A. Carlson, A.F. Gombart, J. Xie, CO2-expanded nanofiber scaffolds maintain activity of encapsulated bioactive materials and promote cellular infiltration and positive host response, Acta Biomater. 68 (2018) 237–248.

[14] S. Chen, H. Wang, A. McCarthy, Z. Yan, H.J. Kim, M.A. Carlson, Y. Xia, J. Xie, Three-dimensional objects consisting of hierarchically assembled nanofibers with controlled alignments for regenerative medicine, Nano Lett. 19 (3) (2019) 2059–2065.

[15] S. Chen, H. Wang, V.L. Mainardi, A. Talò, A. McCarthy, J.V. John, M.J. Teusink, L. Hong, J. Xie, Biomaterials with structural hierarchy and controlled 3D nanotopography guide endogenous bone regeneration, Sci. Adv. 7 (31) (2021) eabg3089.

[16] H. Pan, Y. Wei, C. Zeng, G. Yang, C. Dong, W. Wan, S. Chen, Hierarchically assembled nanofiber scaffold guides long bone regeneration by promoting osteogenic/chondrogenic differentiation of endogenous mesenchymal stem cells, Small (2024) 2309868.

[17] C.Y. Liaw, S. Ji, M. Guvendiren, Engineering 3D hydrogels for personalized in vitro human tissue models, Adv. Healthcare Mater. 7 (4) (2018) 1701165.

[18] H. Cui, T. Esworthy, X. Zhou, S.Y. Hann, R.I. Glazer, R. Li, L.G. Zhang, Engineering a novel 3D printed vascularized tissue model for investigating breast cancer metastasis to bone, Adv. Healthcare Mater. 9 (15) (2020) 1900924.

[19] S. Chen, J.V. John, A. McCarthy, J. Xie, New forms of electrospun nanofiber materials for biomedical applications, J. Mater. Chem. B 8 (17) (2020) 3733–3746.

[20] L. Moroni, J.A. Burdick, C. Highley, S.J. Lee, Y. Morimoto, S. Takeuchi, J.J. Yoo, Biofabrication strategies for 3D in vitro models and regenerative medicine, Nat. Rev. Mater. 3 (5) (2018) 21–37.

[21] C. Cai, H. Zhu, Y. Chen, Y. Guo, Z. Yang, H. Li, H. Liu, Mechanoactive nanocomposite hydrogel to accelerate wound repair in movable parts, ACS Nano 16 (12) (2022) 20044–20056.

[22] G. Singh, A. Chanda, Mechanical properties of whole-body soft human tissues: a review, Biomed. Mater. 16 (6) (2021) 062004.

[23] A.M.J. Coenen, K.V. Bernaerts, J.A.W. Harings, S. Jockenhoevel, S. Ghazanfari, Elastic materials for tissue engineering applications: Natural, synthetic, and hybrid polymers, Acta Biomater. 79 (2018) 60–82.

[24] D.T. Wu, N. Jeffreys, M. Diba, D.J. Mooney, Viscoelastic biomaterials for tissue regeneration, Tissue Eng. C Methods 28 (7) (2022) 289–300.

[25] N. Mangir, B. Aldemir Dikici, C.R. Chapple, S. MacNeil, Landmarks in vaginal mesh development: polypropylene mesh for treatment of SUI and POP, Nat. Rev. Urol. 16 (11) (2019) 675–689.

[26] M. Karon, S. Chatterjee, Sacrocolpopexy: patient outcomes support the use of non-crosslinked acellular dermal matrix as an alternative to the synthetic polypropylene mesh, J. Gynecol. Surg. 35 (6) (2019) 337–344.

[27] M. Pero, C. Castells-Sala, L. Alserawan, L. Casani, J.O. Juan Babot, I. Jorba, M. L. Pérez, E. Moga, J. Otero, P. López-Chicón, Comparison of a human acellular dermal matrix and a polypropylene mesh for pelvic floor reconstruction: a randomized trial study in a rabbit model, Sci. Rep. 12 (1) (2022) 20698.

[28] F.M. Reid, A. Elders, S. Breeman, R.M. Freeman, P.s.g. the, How common are complications following polypropylene mesh, biological xenograft and native tissue surgery for pelvic organ prolapse? A secondary analysis from the PROSPECT trial, BJOG An Int. J. Obstet. Gynaecol. 128 (13) (2021) 2180–2189.

[29] S. Chen, H. Wang, Y. Su, J.V. John, A. McCarthy, S.L. Wong, J. Xie, Mesenchymal stem cell-laden, personalized 3D scaffolds with controlled structure and fiber alignment promote diabetic wound healing, Acta Biomater. 108 (2020) 153–167.

[30] A. Ray, O. Lee, Z. Win, R.M. Edwards, P.W. Alford, D.-H. Kim, P.P. Provenzano, Anisotropic forces from spatially constrained focal adhesions mediate contact guidance directed cell migration, Nat. Commun. 8 (1) (2017) 14923.

[31] M. Monteiro-Soares, D. Russell, E.J. Boyko, W. Jeffcoate, J.L. Mills, S. Morbach, F. Game, F. International Working Group on the Diabetic, Guidelines on the classification of diabetic foot ulcers (IWGDF 2019), Diabetes/metabolism research and reviews 36 (2020) e3273.

[32] J. Mao, L. Chen, Z. Cai, S. Qian, Z. Liu, B. Zhao, Y. Zhang, X. Sun, W. Cui, Advanced biomaterials for regulating polarization of macrophages in wound healing, Adv. Funct. Mater. 32 (12) (2022) 2111003.

[33] H. Kim, S.Y. Wang, G. Kwak, Y. Yang, I.C. Kwon, S.H. Kim, Exosome-guided phenotypic switch of M1 to M2 macrophages for cutaneous wound healing, Adv. Sci. 6 (20) (2019) 1900513.

[34] E.L. Anghel, M.V. DeFazio, J.C. Barker, J.E. Janis, C.E. Attinger, Current concepts in debridement: science and strategies, Plast. Reconstr. Surg. 138 (3S) (2016) 82S–93S.

[35] Z. Tu, M. Chen, M. Wang, Z. Shao, X. Jiang, K. Wang, Z. Yao, S. Yang, X. Zhang, W. Gao, Engineering bioactive M2 macrophage-polarized anti-inflammatory, antioxidant, and antibacterial scaffolds for rapid angiogenesis and diabetic wound repair, Adv. Funct. Mater. 31 (30) (2021) 2100924.

[36] Z. Feng, Q. Su, C. Zhang, P. Huang, H. Song, A. Dong, D. Kong, W. Wang, Bioinspired nanofibrous glycopeptide hydrogel dressing for accelerating wound healing: a cytokine-free, M2-type macrophage polarization approach, Adv. Funct. Mater. 30 (52) (2020) 2006454.